An analysis of flow, temperature, and chemical composition distortion in gas sampling through an orifice during chemical vapor deposition

Mark T. Swihart[a] and Steven L. Girshick
Department of Mechanical Engineering, University of Minnesota, Minneapolis, Minnesota 55455

(Received 22 May 1998; accepted 17 December 1998)

Measurement of the chemical composition of gases sampled through a small hole in the substrate can be a useful diagnostic for investigations of the chemistry of chemical vapor deposition (CVD) processes. Ideally, one would measure the composition of the gas at the growth surface. However, the flow disturbance due to sampling causes the conditions at the mouth of the orifice to be different from those at the growth surface. Unless the orifice diameter is sufficiently small, relative to the thickness of chemical and thermal boundary layers above the growth surface, the sampled composition will differ from the composition at the growth surface. In this work, we present results of two-dimensional simulations of the flow, heat transfer, and chemical reactions in an axisymmetric stagnation point flow with gas sampling through a small orifice in the substrate on the symmetry axis of the flow field. Detailed results are given for atmospheric-pressure radio-frequency plasma CVD of diamond, corresponding to experiments performed in our laboratory. We also present more general results, approximate analytical representations of the flow field, and scaling rules for the size of the disturbance due to the sampling orifice. © *1999 American Institute of Physics.* [S1070-6631(99)01204-0]

I. INTRODUCTION

Gas sampling through an orifice in the substrate, followed by gas chromatographic or mass spectrometric analysis of the sampled gases, has been used to investigate the chemistry of a wide range of chemical vapor deposition (CVD) processes. Systems where this technique has been applied include combustion CVD of diamond,[1] hot filament CVD of diamond,[2] atmospheric-pressure radio-frequency plasma CVD of diamond,[3–5] microwave plasma CVD of diamond,[6] plasma-enhanced CVD of diamondlike carbon,[7] laser-assisted CVD of germanium,[8] thermal CVD of AlN from $((CH_3)_2AlNH_2)_3$,[9] MOCVD of GaAs,[10,11] photo-assisted CVD of Si_3N_4,[12] tungsten CVD,[13] and laser-induced CVD of amorphous hydrogenated silicon.[14] In several of these studies,[1,2,4] measured concentrations were explicitly compared to one-dimensional simulations of a chemically reacting stagnation point flow computed using the SPIN code[15] from Sandia National Laboratories. In other cases, though such explicit comparisons were not made, the composition of the gas entering the sampling orifice was assumed to be identical to the composition at the film surface. This neglects any effects that the flow into the orifice has on the flow, temperature, and concentration fields in its vicinity.

Our interest in exploring the effect of these sampling distortions arises from the experimental and modeling studies of atmospheric-pressure radio-frequency plasma CVD of diamond performed previously in our laboratory.[4,5,16,17] In these experiments, diamond was deposited on a molybdenum substrate at atmospheric pressure using a radiofrequency induction plasma operating with argon as the main plasma gas. Methane and hydrogen were the reactants, with typical inlet CH_4:H_2:Ar ratios of 1:50:500. Gases were sampled through a 70 μm orifice at the center of the substrate and analyzed by gas chromatography. A two-dimensional model of the plasma[17] predicted peak temperatures above 10 000 K. For typical conditions, that model predicted that the 4000 K isotherm is approximately 2 mm from the substrate. A one-dimensional stagnation point flow model was used to model the deposition and boundary layer chemistry, with the freestream conditions obtained from the predictions of the two-dimensional plasma model at the 4000 K isotherm. The freestream composition was taken as an equilibrium mixture of Ar, H, H_2, and the C_1 and C_2 hydrocarbons at 4000 K and 1 atm.[17] A third model predicted composition changes in the sampling line to the gas chromatograph.[4,18] The stagnation point flow model predicts chemical boundary layer thicknesses comparable to the orifice diameter for some species. It was also found that the predicted concentrations at a distance of 200 μm above the substrate surface were in much better agreement with the measured concentrations than were the predicted concentrations at the surface.[4] This suggests that sampling distortions due to the flow into the orifice are important in this system.

Sampling distortions in molecular beam mass spectrometry (MBMS) of reactive species in flames have been considered by several authors. Flame sampling is a similar, but not identical problem to the one considered here. In flame sampling, the goal is to obtain the composition of the unperturbed flame, the situation that would exist if no sampling

[a]Author to whom correspondence should be addressed. Fax: (716)645-3822. Current address: Department of Chemical Engineering, University at Buffalo (SUNY), Buffalo, New York 14260-4200. Electronic mail: swihart@eng.buffalo.edu.

probe were present at all and, therefore, no surface reactions occurred. In sampling through a CVD substrate, the goal is to measure the concentrations that would exist at the surface if it did not have a hole in it, with the surface reactions undisturbed. What the two situations have in common is a shifting of the isotherms and composition profiles toward the sampling orifice due to the flow into it. An early analysis of MBMS sampling from flames was presented by Hayhurst, Kittelson, and Telford,[19–21] who used simple analytical approximations to the flow field to estimate the disturbance of the flame due to flow into the probe and due to the boundary layer formed near the probe entrance. Later, Yi and Knuth[22] studied the shift of concentration profiles due to flow into a sampling cone by performing two-dimensional calculations for inviscid flow, diffusion, and a single first order chemical reaction in a binary mixture. Knuth,[23] and Smith[24] have reviewed these and many other studies of composition distortions in MBMS sampling.

One goal of the present work was to quantitatively determine the effect of distortions due to flow into the sampling orifice on measured species concentrations during atmospheric-pressure radio-frequency plasma CVD of diamond under the conditions used in our laboratory. An additional objective was to generalize these results to allow simple calculation of the approximate extent of the sampling disturbance under conditions relevant to other CVD processes. To do this, we have performed two-dimensional simulations of the near-orifice region of a stagnation point flow in which there is critical flow through a small orifice located on the axis of the flow. For conditions corresponding to experiments from this laboratory that have been presented previously,[4,5] simulations that included detailed diamond CVD chemistry in both the gas phase and on the surface were carried out. To generalize the results, we also performed less computationally expensive simulations, including only three species and a single surface reaction, over a range of pressures, total flow rates, orifice diameters, and freestream and substrate temperatures. These results are compared to results based on simple, analytical streamfunction representations similar to those used by Hayhurst, Kittelson, and Telford.[19] Approximate scaling rules for the size of the sampling disturbance are obtained from the results. These can be used to estimate the effects of sampling under other conditions.

II. SIMULATION METHODOLOGY

The numerical simulations presented in this work were carried out using the commercial finite volume based computational fluid dynamics code CFD-ACE.[25] The solution procedure used in this code is essentially that presented by Patankar,[26] with the additional capabilities of using multiple domains, body fitted coordinates, and higher-order differencing schemes. The equations solved were the mixture continuity equation, the axial and radial momentum conservation equations, the energy conservation equation, a continuity equation for each gas phase chemical species, and a surface species conservation equation for all but one of the surface species. These equations are summarized in Table I. In this work, first order upwinded differences were used for the density, second order upwinded differences were used for the velocity components, and central differences were used for the enthalpy and species mass fractions. The flow was treated as compressible, and variations of thermodynamic and transport properties with temperature, pressure, and composition were accounted for. Temperature and composition dependent mixture viscosity, thermal conductivity, mixture-averaged diffusion coefficients, and thermal diffusion coefficients were obtained from the kinetic theory of gases[27] with Lennard-Jones parameters taken from the CHEMKIN transport property library.[28] Thermodynamic properties of the chemical species were taken from the CHEMKIN thermodynamic database.[29] The CFD-ACE program was augmented with routines to allow calculation of the thermal diffusion coefficients using the rigorous methods of the CHEMKIN transport package,[28] and with routines to solve for the fractional coverages of the surface species and to couple the rates of surface reactions to the gas phase species continuity equations through their boundary conditions at the growth surface. SURFACE CHEMKIN[30] was used to manage the surface reaction mechanism and to compute reaction rates of surface reactions, while the built-in capabilities of CFD-ACE were used to handle the gas phase chemistry. The computational domain is sketched in Fig. 1, where we have indicated the boundary conditions used. This geometry corresponds to the sampling orifice used in the experiments presented in previous work from this laboratory.[4,5]

For simulations used to obtain quantitative results corresponding to experiments performed in our laboratory (see above), detailed reaction mechanisms were used in both the gas phase and on the surface. In the gas phase, a mechanism consisting of 27 reactions among 16 species (H_2, H, Ar, and the C_1 and C_2 hydrocarbons) was used. This reduced mechanism was obtained from the larger set of reactions reported elsewhere[31] by application of the mechanism reduction based on principal component analysis.[32] The larger mechanism upon which this reduced mechanism is based contains the hydrocarbon reactions found in the GRI mechanism for methane combustion[33] augmented by additional reactions involving atomic carbon, and with some rate parameters updated based on more recent results. The extended growth-by-methyl mechanism of Yu and Girshick,[16] based on the Harris mechanism,[34] was used at the diamond deposition surface. Simpler simulations were also performed, in which only H, H_2, and Ar were included, and the only chemical reaction was H atom recombination at the surface with a recombination coefficient of 0.16.

For the simulations including detailed chemistry, the expanding portion of the domain downstream of the sampling orifice was omitted. The pressure profile at the orifice exit calculated without detailed chemistry was imposed as a boundary condition for the simulations that included detailed chemistry. The velocity profile at the orifice outlet obtained using this pressure boundary condition was identical to that obtained with the larger domain. Solutions of the quasi-one-dimensional stagnation point flow problem, for comparison to the two-dimensional results, were obtained using the SPIN code from the CHEMKIN package.[15] These included the same

TABLE I. Governing equations.[a]

Mixture continuity

$$\frac{1}{r}\frac{\partial}{\partial r}(\rho r v)+\frac{\partial}{\partial z}(\rho u)=0$$

Radial momentum

$$\rho\left(v\frac{\partial v}{\partial r}+u\frac{\partial v}{\partial z}\right)+\frac{\partial p}{\partial r}+\frac{1}{r}\frac{\partial}{\partial r}(r\tau_{rr})+\frac{\partial \tau_{rz}}{\partial z}-\frac{\tau_{\theta\theta}}{r}=0$$

Axial momentum

$$\rho\left(v\frac{\partial u}{\partial r}+u\frac{\partial u}{\partial z}\right)+\frac{\partial p}{\partial z}+\frac{1}{r}\frac{\partial}{\partial r}(r\tau_{rz})+\frac{\partial \tau_{zz}}{\partial z}=0$$

Energy

$$\rho C_p\left(v\frac{\partial T}{\partial r}+u\frac{\partial T}{\partial z}\right)-\frac{1}{r}\frac{\partial}{\partial r}\left(r\lambda\frac{\partial T}{\partial r}\right)-\frac{\partial}{\partial z}\left(\lambda\frac{\partial T}{\partial z}\right)+\sum_{k=1}^{K_g}\left(\rho C_{p_k}Y_k\left(U_k\frac{\partial T}{\partial z}+V_k\frac{\partial T}{\partial r}\right)+\dot{\omega}_k h_k\right)+v\frac{\partial p}{\partial r}+u\frac{\partial p}{\partial z}=0$$

Species continuity

$$\rho\left(v\frac{\partial Y_k}{\partial r}+u\frac{\partial Y_k}{\partial z}\right)+\frac{1}{r}\frac{\partial}{\partial r}(r\rho Y_k V_k)+\frac{\partial}{\partial z}(\rho Y_k U_k)+M_k\dot{\omega}_k=0,\quad k=1,\ K_g-1$$

$$Y_{K_g}=1-\Sigma_{k=1}^{K_g-1}Y_k$$

Surface site conservation

$$\dot{s}_k=0,\quad k=1,\ K_s-1$$

$$\theta_{K_s}=1-\Sigma_{k=1}^{K_s-1}\theta_k$$

where

$$\tau_{rr}=-\mu\left(2\frac{\partial v}{\partial r}-\frac{2}{3}\left(\frac{1}{r}\frac{\partial}{\partial r}(rv)+\frac{\partial u}{\partial z}\right)\right)$$

$$\tau_{\theta\theta}=-\mu\left(2\frac{v}{r}-\frac{2}{3}\left(\frac{1}{r}\frac{\partial}{\partial r}(rv)+\frac{\partial u}{\partial z}\right)\right)$$

$$\tau_{zz}=-\mu\left(2\frac{\partial u}{\partial z}-\frac{2}{3}\left(\frac{1}{r}\frac{\partial}{\partial r}(rv)+\frac{\partial u}{\partial z}\right)\right)$$

$$\tau_{rz}=-\mu\left(\frac{\partial u}{\partial r}+\frac{\partial v}{\partial z}\right)$$

$$V_k=-\frac{1}{X_k}D_{km}\frac{dX_k}{dr}-\frac{D_k^T}{\rho Y_k}\frac{1}{T}\frac{\partial T}{\partial r},\quad k=1,\quad K_g-1$$

$$U_k=-\frac{1}{X_k}D_{km}\frac{dX_k}{dz}-\frac{D_k^T}{\rho Y_k}\frac{1}{T}\frac{\partial T}{\partial z},\quad k=1,\quad K_g-1$$

$$V_{K_g}=\frac{1}{Y_{K_g}}\left(1-\sum_{k=1}^{K_g-1}Y_kV_k\right)\qquad U_{K_g}=\frac{1}{Y_{K_g}}\left(1-\sum_{k=1}^{K_g-1}Y_kU_k\right)$$

[a] r=radial coordinate, z=axial coordinate, u=axial velocity, v=radial velocity, T=temperature, ρ=density, p=pressure, Y_k=mass fraction of species k, X_k=mole fraction of species k, θ_k=fractional coverage of surface species k, h_k=molar enthalpy of species k, τ=stress tensor, $\dot{\omega}_k$=molar production rate of species k by gas phase reactions, K_g=number of gas phase species, $\dot{s}_k$=molar production rate of species k by surface reactions, K_s=number of surface species, C_p=mixture specific heat, C_{pk}=specific heat of species k, λ=mixture thermal conductivity, U_k=axial diffusion velocity of species k, V_k=radial diffusion velocity of species k, D_{km}=mixture-averaged diffusion coefficient of species k in the mixture, M_k=molecular weight of species k, D_k^T=thermal diffusion coefficient for species k.

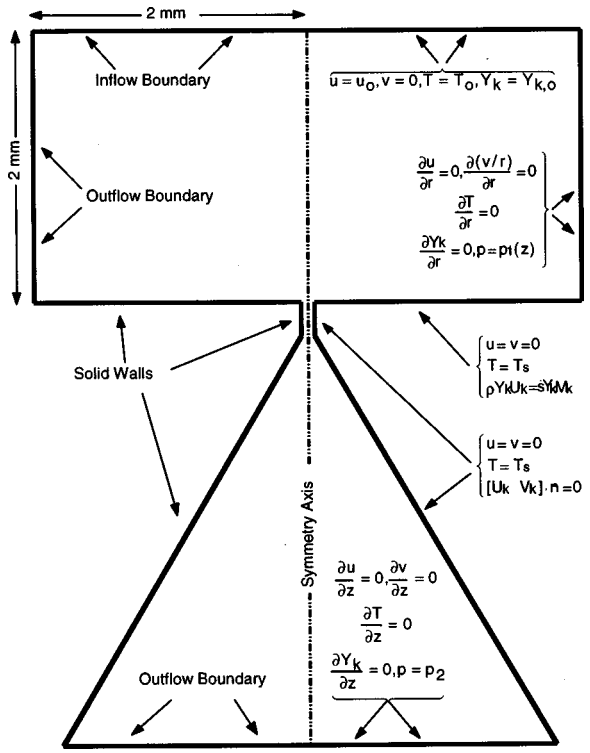

FIG. 1. Sketch of computational domain showing the boundary conditions applied. Variables are defined in Table I.

chemistry as the two-dimensional simulations. The pressure profile boundary condition applied along the radial outflow boundary of the domain [$p_1(z)$ in Fig. 1] was obtained by integration of the axial momentum equation for the quasi-one-dimensional stagnation point flow using the velocity, density, and viscosity profiles predicted by the SPIN code. Therefore the imposed pressure boundary condition was the pressure profile that would be present in an ideal stagnation point flow. This boundary condition was necessary to achieve quantitative agreement between the quasi-one-dimensional solution and the two-dimensional simulations at points radially distant from the orifice.

III. RESULTS AND DISCUSSION

A. Typical results

Typical isotherms and streamlines are shown in Fig. 2. These are for a freestream velocity (u_0) of 10 m/s, an upstream pressure [$p_0=p_1(z=0)$] of 1 atm, a freestream temperature (T_0) of 4000 K, a wall temperature (T_w) of 1200 K, an orifice diameter of 70 μm, and a downstream pressure (p_2) of 20 Torr. These are conditions corresponding to the experiments and calculations presented by Girshick, Li, Yu, and Han.[17] Only the streamlines near the orifice are shown. The streamlines are those of an ideal stagnation point flow, except near the sampling orifice. Likewise, the isotherms (and concentration isolines, not shown) are parallel to the substrate far from the orifice, as they would be in an ideal stagnation point flow. Compressibility effects are not signifi-

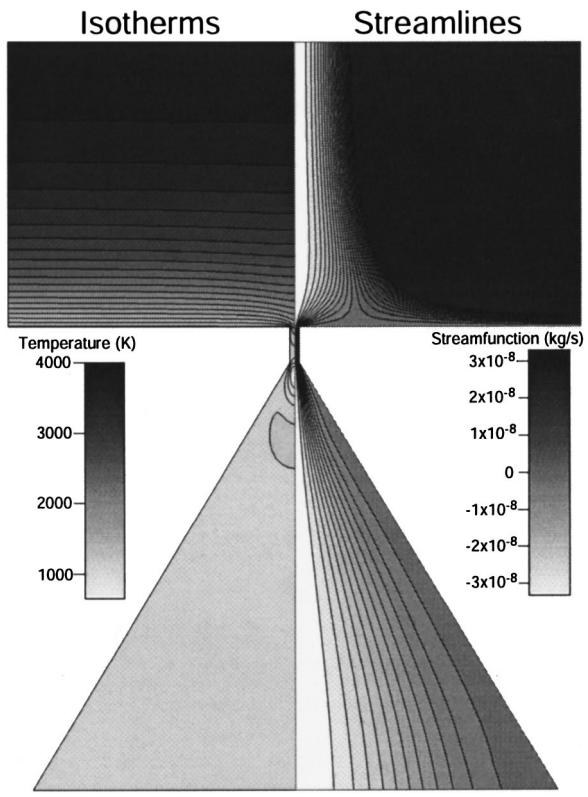

FIG. 2. Typical flow and temperature fields from two-dimensional simulations. Boundary conditions are $T_0=4000$ K, $u_0=10$ m/s, $p_0=1$ atm, $T_s=1200$ K, $p_2=20$ Torr.

cant in the region upstream of the orifice. For the conditions of Fig. 2, the Mach number is 0.38 at the center of the orifice mouth and the pressure is 0.89 atm.

Under all conditions considered here, the flow through the orifice is choked and reaches a Mach number of $M=1$ just before the orifice outlet. For the conditions of Fig. 2, the total mass flow through the orifice is about 2.1×10^{-7} kg/s. The maximum gas velocity is about 1100 m/s ($M=2.1$), on the centerline, about 0.1 mm past the orifice exit. This expansion is followed by a recompression with slight overcompression, then relaxation to the final pressure. This is the expected behavior downstream of the orifice. For the conditions of Fig. 2, the first shock (expansion) was located about 0.03 mm before the orifice outlet, and the second shock (recompression) was about 0.35 mm past the orifice outlet, on the centerline. Due to boundary layers on the walls, these shocks were not perpendicular to the walls. Since our focus was on the behavior upstream of the orifice, we did not attempt to sharply resolve these shocks. The length of the domain downstream of the orifice did not affect the flow, provided that it was sufficiently long that radial pressure gradients could be neglected and a constant pressure boundary condition could be specified at the outlet. The downstream pressure did not affect the flow upstream of the orifice. Changing the downstream pressure by a factor of 2 in either direction changed the mass flowrate into the orifice by less than 0.1%. The downstream flow will not be considered further, since it does not significantly affect the flow upstream of the orifice.

For the conditions of Fig. 2, the separation streamline between flow that enters the orifice and flow that exits radially meets the substrate at about 0.4 mm from the symmetry axis. The radial position of this stagnation ring (hereafter denoted R_{st}) is one measure of the size of the disturbance due to sampling. Significant distortion of the isotherms is observed near the orifice. The radial extent of this distortion is comparable to the stagnation ring location, R_{st}. Another measure of the size of the disturbance is the axial distance by which the isotherms are shifted at the center of the orifice. We define this shift (hereafter denoted δ_T) as the distance from the substrate, at points radially distant from the orifice, for which the temperature is equal to the temperature at the center of the orifice. For the case shown in Fig. 2, this shift is about 70 μm. There are corresponding shifts of the concentration isolines for each chemical species. The distortions in the concentration profiles are coupled to each other and to the distortions in the temperature profile by gas phase reactions, since the rates of these reactions are highly temperature dependent. These shifts in the isotherms and concentration isolines will significantly affect the concentration of a species entering the orifice if they are comparable to the thickness of the chemical boundary layer for that species.

B. Results from simulations with detailed chemistry

As described above, simulations including detailed chemistry corresponding to the diamond deposition experiments described by Lindsay, Larson, and Girshick[5] were performed to determine quantitatively the effect of the sampling disturbance in those experiments. Figure 3 shows results of calculations corresponding to deposition at a substrate temperature of 1200 K, a pressure of 1 atm, an orifice diameter of 70 μm, and an input methane to hydrogen ratio of 2%. Figure 4 shows corresponding axial species profiles on the axis of symmetry and 2 mm from the axis of symmetry for several compounds of interest in diamond deposition. For acetylene, shown on the left-hand side of Fig. 3, the concentration boundary layer is thick compared to the size of the sampling disturbance, and the acetylene mole fraction at the orifice is only slightly different from its value at the growth surface away from the orifice. However, methane is formed in a boundary layer whose thickness is comparable to the dimensions of the sampling disturbance, and therefore its mole fraction at the orifice is substantially different from its value at the growth surface. Similar observations can be made for the other species shown in Fig. 4. Mole fractions of all of the species at the orifice center, at the growth surface, and averaged over the flow through the orifice are given in Table II. The difference between the mole fractions of species at the growth surface and at the orifice ranges from about 2% for argon, H_2, and C_2H_2, to several orders of magnitude for trace species that are formed or destroyed in a very thin region near the surface.

For each species we can define an effective sampling distance (δ_k) as the distance from the substrate, at points radially distant from the orifice, where its mole fraction is equal to its mole fraction at the center of the orifice. Table II presents these effective sampling distances. These range

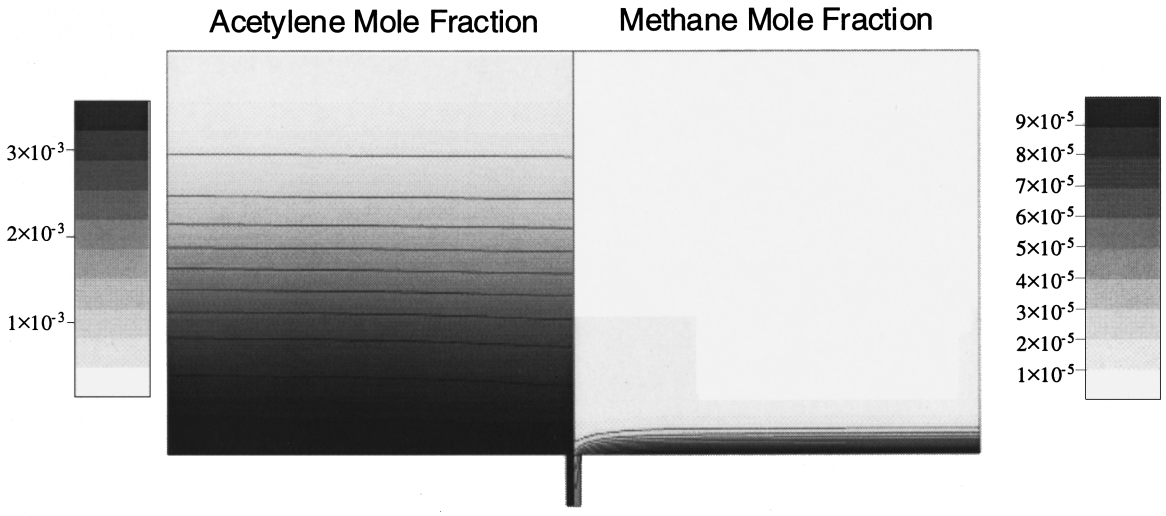

FIG. 3. Acetylene and methane concentration profiles from two-dimensional simulations including detailed gas phase and surface chemistry. Conditions are the same as in Fig. 2. The freestream composition is an equilibrium mixture of the sixteen species considered at 4000 K and 1 atm with atom fractions of 40.3% H, 59.1% Ar, and 0.54% C.

from 31 to 160 μm, depending on the diffusion coefficient of the species, its unperturbed concentration profile, and how it is coupled to the other species by reaction. The corresponding shift in the isotherms (δ_T as defined above) is 60 μm. This is comparable to the shifts in the concentration isolines for most of the species. Yi and Knuth[22] found, in their simulations of flow into an orifice at the tip of a sampling cone, that the effective sampling distance for species whose characteristic reaction time was larger than the characteristic flow time was approximately given by

$$\frac{\delta_k}{d} = \alpha \, \mathrm{Pe}_{m,k}^{0.5}, \tag{1}$$

where d=orifice diameter, $\mathrm{Pe}_{m,k}$=Peclet number for mass transfer=$\mathrm{Re}\,\mathrm{Sc}_k = u_{\mathrm{or}} d/D_{km}$, u_{or}=average velocity at the orifice, D_{km}=mixture-averaged diffusion coefficient for species k, α=a constant of proportionality, 0.19 in Yi and Knuth's work.[22]

The final column of Table II gives the value of δ_k from this expression for each species, with the constant of proportionality set at $\alpha = 0.163$, which gave the best agreement with the detailed calculations when H_2, Ar, CH_2, CH_3, and C_2H_2 were excluded (see footnotes to Table II). For these species, there is reasonable agreement between the prediction from Eq. (1) and the observed value of (δ_k). Thus, Eq. (1) can give a useful, semiquantitative estimate of the sampling distance for species that have a significant concentration gradient near the surface and for which the concentration increases or decreases monotonically over a distance of a few orifice diameters from the surface. The concentrations of species without a significant concentration gradient near the surface will be unaffected.

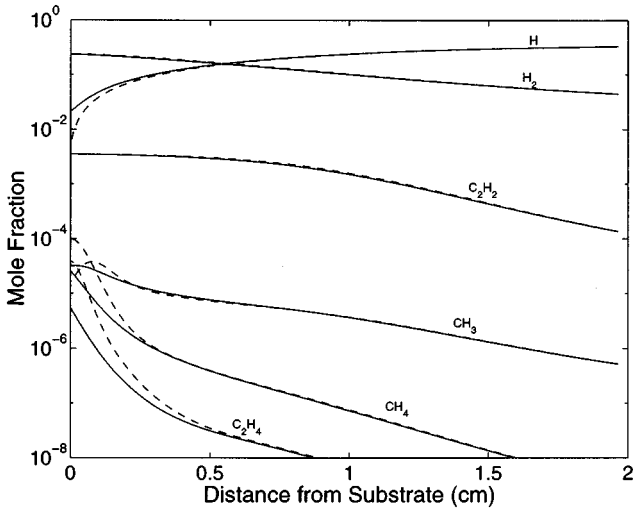

FIG. 4. Concentration profiles for several important species in diamond deposition from the same simulation presented in Fig. 3. Solid lines are the axial profiles at radial positions far from the orifice, and the dashed lines are the profiles along the symmetry axis.

We would expect the effective sampling distance to depend only on the Peclet number if the only processes governing the species concentrations were convection and molecular diffusion. In this reactive flow, gas phase reactions, surface reactions, and thermal diffusion lead to dependence on other dimensionless quantities in addition to the Peclet number. In principle, the effective sampling distance for each component should depend on its thermal diffusion ratio [which can be defined as $k_T = D_k^T/(\rho Y_k D_{km})$ in a multicomponent system], its gas phase Damköhler number [defined as $\mathrm{Da}_g = (\dot{\omega}_k d^2)/(c_k D_{km})$] and its surface Damköhler number [defined as $\mathrm{Da}_s = (\dot{s}_k d)/(c_k D_{km})$]. These numbers are defined based on reaction rates and diffusion coefficients at a particular location. It may not be possible to define a representative production rate ($\dot{\omega}_k$) for a species, since that quantity may change by orders of magnitude over distances comparable to the orifice diameter. We evaluated these three dimensionless groups using the concentrations, properties, and production rates at the substrate surface and examined the dependence of the effective sampling distance on them.

TABLE II. Species concentrations.

Species	Mole fraction at orifice center	Mole fraction averaged over outflow	Mole fraction at surface	Effective sampling distance (δ_k) (μm)	Estimated δ_k from Eq. (1) (μm)
H_2	2.31×10^{-1}	2.34×10^{-1}	2.37×10^{-1}	a	38
CH_4	2.71×10^{-5}	3.93×10^{-5}	9.87×10^{-5}	88	74
C_2H_4	5.90×10^{-6}	1.13×10^{-5}	3.83×10^{-5}	82	86
Ar	7.44×10^{-1}	7.43×10^{-1}	7.54×10^{-1}	a	160
CH_3	3.12×10^{-5}	2.84×10^{-5}	1.84×10^{-5}	43[b]	74
H	2.12×10^{-2}	1.97×10^{-2}	5.31×10^{-3}	46	31
C_2H_6	5.72×10^{-9}	2.30×10^{-8}	1.79×10^{-7}	81	90
C	5.05×10^{-5}	4.39×10^{-5}	1.07×10^{-5}	89	64
CH	1.76×10^{-6}	1.32×10^{-6}	1.69×10^{-7}	88	60
$^3CH_2$	5.98×10^{-6}	4.95×10^{-6}	2.63×10^{-6}	153[c]	73
C_2	1.96×10^{-8}	1.24×10^{-8}	5.18×10^{-10}	81	76
C_2H	4.74×10^{-7}	2.77×10^{-7}	6.34×10^{-9}	61	85
C_2H_2	3.57×10^{-3}	3.54×10^{-3}	3.49×10^{-3}	a	85
C_2H_3	5.38×10^{-6}	8.54×10^{-6}	1.62×10^{-5}	85	86
C_2H_5	6.98×10^{-9}	2.24×10^{-8}	1.50×10^{-7}	80	90
$^1CH_2$	1.12×10^{-7}	7.81×10^{-8}	9.22×10^{-9}	58	73

[a]The effect of the sampling disturbance on the concentrations of these species is negligible.
[b]CH_3 behaves anomolously because its unperturbed concentration profile goes through a maximum about 80 μm from the surface.
[c]CH_2 behaves anomolously because its unperturbed concentration profile goes through a minimum about 25 μm from the surface.

The effective sampling distance appeared to correlate with Da_g and with k_T, but we do not have a sufficient number of results over a large enough range of these parameters to make any general statements about this dependence. The effective sampling distance did not appear to depend significantly on Da_s, but again there is insufficient information to generalize.

In previous modeling of the diamond deposition experiments to which these calculations correspond,[4] it was found that there was significant disagreement between the concentrations measured in a sample withdrawn through the 70 μm orifice and the predictions of the gas phase concentrations at the surface obtained from a one-dimensional boundary layer model that did not account for perturbations due to the flow into the sampling orifice. It was speculated that this difference might be due to sampling effects. This hypothesis was based on the observation that the measured concentrations agreed reasonably with the gas phase concentrations predicted by the model at a position 200 μm above the growth surface. The simulations presented here, and others not presented, showed that sampling effects could not fully account for the discrepancies. However, they also showed that sampling effects were significant, and that inclusion of these effects moves the model predictions closer to agreement with the experimental observations. For example, as seen in Table II, sampling effects can cause the sampled CH_4 concentration to differ from the concentration at the surface by more than a factor of 2. The previous calculations used the reaction mechanisms presented by Yu and Girshick[16] and by Lindsay.[18] More recent calculations,[31] that used the same reaction mechanism as the present work, showed that the bulk of the discrepancy between the model and experiment was due to inadequacy of the gas phase reaction mechanism used. The revised reaction mechanism, when sampling effects are also properly accounted for, gives good agreement with the experimentally measured concentrations of the stable hydrocarbons.[31]

C. Comparison of detailed simulations to simplified streamfunction expressions

The flow field from the two-dimensional simulations presented here can be reasonably approximated by an analytical streamfunction. In their analysis of sampling effects in molecular beam mass spectrometry from flames, Hayhurst, Kittelson, and Telford[19] approximated the flow field using the superposition of the streamfunctions for inviscid, incompressible flow against a flat plate and into a point sink. If we adopt the same approach, the streamfunction and corresponding velocity components are

$$\psi(r,z)=2kr^2z-\frac{mz}{\sqrt{r^2+z^2}}, \tag{2}$$

$$\rho u=-\frac{1}{r}\frac{\partial\psi}{\partial r}=-4kz-\frac{mz}{(r^2+z^2)^{3/2}}, \tag{3}$$

$$\rho v=\frac{1}{r}\frac{\partial\psi}{\partial z}=2kr-\frac{mr}{(r^2+z^2)^{3/2}}, \tag{4}$$

where $\psi(r,z)$=streamfunction (lines of constant ψ are streamlines); r=radial coordinate; z=axial coordinate, with the orifice in the $z=0$ plane; ρ=density; u=axial velocity;

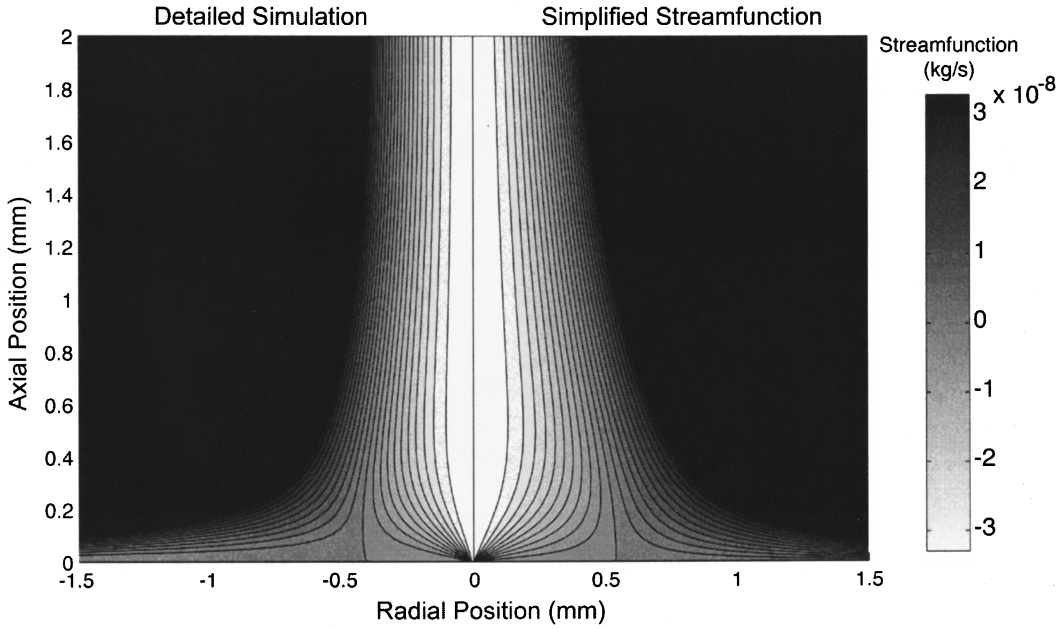

FIG. 5. Comparison of streamlines from a complete two-dimensional simulation to the simplified streamfunction given by Eq. (2) in the text. Boundary conditions are $T_0=4000$ K, $u_0=10$ m/s, $p_0=1$ atm, $T_s=1200$ K, $p_2=20$ Torr.

v=radial velocity; $m=\dot{m}/(2\pi)$=(total mass flow rate into sink)/(2π); $k=-(\rho_0 u_0)/(4z_0)$; and ρ_0, u_0=density and axial velocity in a reference plane at $z=z_0$.

The first term on the right-hand side of each expression describes the flow against an infinite plane, and the second term describes flow into a point sink. The streamfunction formulation guarantees satisfaction of the overall continuity equation, but the velocity components are not required to satisfy any momentum balances. Figure 5 compares the streamlines from the above streamfunction to those from the detailed simulation for the same conditions described in the previous section. The sink strength (m) was set to match the flow rate through the orifice from the two-dimensional numerical simulations, and the reference plane ($z=z_0$) was taken to be 2 mm from the substrate. This was the inflow boundary location for the detailed simulations. This simplified streamfunction gives a reasonable approximation to the flow field. A useful result from the simplified streamfunction is the simple scaling rule that it provides for the size of the disturbance in the flow field. The location of the stagnation ring (R_{st}) can be obtained by solving for the radial position of the stagnation streamline ($\psi=0$) and taking the limit as z goes to zero. This gives

$$R_{st}=\left(\frac{m}{2k}\right)^{1/3}, \tag{5}$$

which upon substitution of expressions for m and k gives the dependence of the radial extent of the flow disturbance on operating parameters such as temperatures, freestream velocity, pressure, orifice diameter, etc.

The above streamfunction may be improved to give better agreement with the flow field from the detailed simulations by making modifications that require it to satisfy more physically realistic boundary conditions. For predicting the axial extent of the disturbance, it seems particularly important that the streamfunction result in a velocity field that has zero radial velocity at the substrate surface so that it satisfies the no-slip boundary condition there. Several modifications to Eq. (2) that satisfy appropriate boundary conditions for this problem ($\psi=u=v=0$ at $z=0$, $\psi=-m$ and $v=0$ at $r=0$, and $\psi=2kr^2z$ at $z=z_0$) were investigated. The simplest expression that was found to give significantly improved agreement with the numerical simulations was

$$\psi(r,z)=2kr^2z\left((\alpha-2)\left(\frac{z}{z_0}\right)^3+(3-2\alpha)\left(\frac{z}{z_0}\right)^2+\alpha\frac{z}{z_0}\right)-\frac{mz^2}{\sqrt{(r^2+z^2)((\beta r)^2+z^2)}}, \tag{6}$$

where α and β are dimensionless constants.

We treat the dimensionless numbers α and β as free parameters that may be used to match this streamfunction to those from the detailed simulations. Constant values of $\alpha=9$ and $\beta=1$ gave good results for the range of conditions studied in this work (see below). Figure 6 compares this streamfunction (with $\alpha=9$ and $\beta=1$) to the detailed simulation results for the same conditions shown in Fig. 5. The agreement is much improved, particularly for the location of the stagnation streamline. Similar agreement was observed for a range of other conditions, using the same values of α and β. This expression predicts that the radial position of the stagnation ring will be given by

$$R_{st}=\left(\frac{mz_0}{2\alpha\beta k}\right)^{1/4} \tag{7}$$

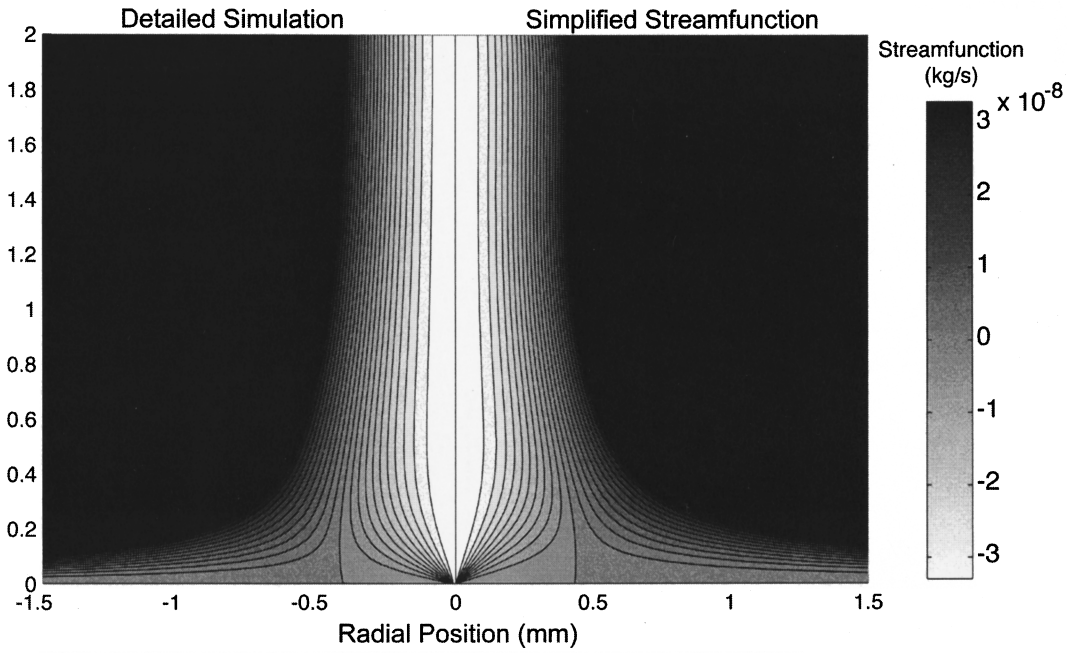

FIG. 6. Comparison of streamlines from a complete two-dimensional simulation to the simplified streamfunction given by Eq. (6) in the text. Boundary conditions are $T_0=4000$ K, $u_0=10$ m/s, $p_0=1$ atm, $T_s=1200$ K, $p_2=20$ Torr. Parameter values in Eq. (6) are $\alpha=9$, $\beta=1$.

which has a slightly weaker dependence of R_{st} on the operating parameters than expression (5).

D. Predicted and observed scaling of the flow disturbance

To predict the size of the flow disturbance, we first need to calculate the mass flow rate through the orifice ($\dot{m}$). For isentropic, adiabatic choked flow through an orifice of diameter d, the mass flow rate is given by[35]

$$\dot{m}=\left(\frac{2}{\gamma+1}\right)^{[(\gamma+1)/2(\gamma-1)]}\sqrt{\frac{\gamma M}{RT_0}}\,(\pi d^2)p_0, \tag{8}$$

where γ is the specific heat ratio, M is the molecular weight of the gas, R is the universal gas constant, T_0 is the upstream temperature, and p_0 is the upstream pressure. Since a real flow is neither isentropic nor adiabatic, the actual mass flow will be lower. Equation (8) is generally multiplied by a discharge coefficient (C_D), which is an empirical factor relating the observed flow rate to the theoretical flow rate from (8). C_D depends on the orifice geometry and the flow conditions. Measurements and correlations for C_D for different orifice geometries and conditions are available in the literature.[36,37] Comparing results of our detailed flow simulations to Eq. (8), with T_0 and γ evaluated at the substrate temperature, gave discharge coefficients in the range $C_D=0.08$ to $C_D=0.56$. As can be seen in Fig. 7, the discharge coefficient was found to scale with the square root of the Reynolds number. In this figure, both the Reynolds number and Eq. (8) were evaluated using conditions at the substrate surface. Of course, this scaling cannot be obeyed for large values of the Reynolds number, since as $\mathrm{Re}\to\infty$, the discharge coefficient must go to one (frictional losses will be negligible). For the orifice geometry considered here, this correlation allows us to estimate the discharge coefficient, and therefore the flow through the orifice. Note that an iterative process is required, since the Reynolds number depends on the flow through the orifice. It is also easy to measure the total flow into the orifice experimentally. In the remainder of this work, we will

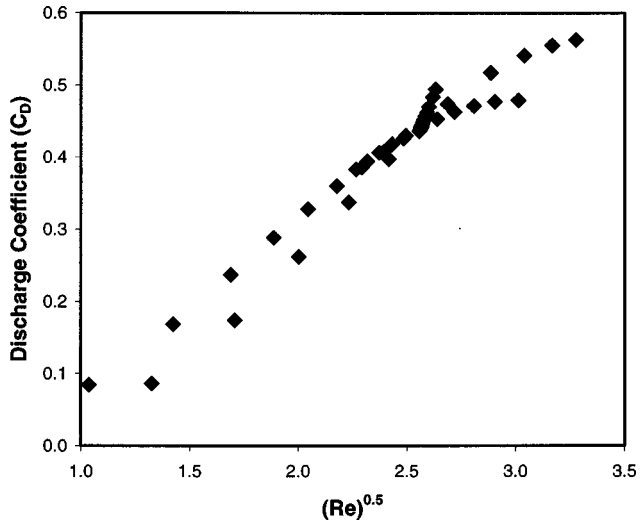

FIG. 7. Dependence of the discharge coefficient on the Reynolds number. The Reynolds number for the flow into the orifice is defined as $(4\dot{m}/\pi d\mu)$, where $\dot{m}$ is the mass flow rate into the orifice, d is the orifice diameter, and μ is the dynamic viscosity (evaluated at the conditions at the substrate surface).

assume that the mass flow rate through the orifice ($\dot{m}$) is known, either from a correlation like the one in Fig. 7 or from experiment.

To test the expected variation of the sampling disturbance with reactor conditions, a set of fifty simulations was conducted with only three chemical species (H, H_2, and Ar), no gas phase reactions, and only hydrogen recombination at the substrate surface. The base conditions for these simulations were those given above for the simulations that included detailed chemistry. These correspond to our atmospheric pressure radio-frequency plasma CVD system, where the boundary layer above the substrate is quite thin and these sampling effects are more likely to be important than in lower temperature systems. Five parameters (p_0, d, u_0, T_0, and T_s) were independently varied, and measures of the size of the sampling disturbance predicted by the numerical simulations were compared to simple scaling rules. The location of the stagnation ring (R_{st}) is a good measure of the radial extent of the disturbance, and can be predicted from Eq. (5) or (7). Figure 8 compares those predictions to the predictions of the detailed numerical simulations for variation of R_{st} with pressure (p_0), orifice diameter (d), freestream velocity (u_0), substrate temperature (T_s), and freestream temperature (T_0). The solid lines are the predictions from (5), and the dashed lines are those from (7). For this range of conditions, these expressions capture essentially the correct dependence of the radial extent of the sampling disturbance on these five parameters. This allows us to predict, at least semiquantitatively, the radial size of the sampling disturbance and, using Eq. (4) or (6), to obtain an approximate flow field for arbitrary conditions.

As can be seen from Eqs. (5) and (7), the location of the stagnation ring depends on the ratio of the strength of the flow into the orifice (of which m is a measure) to the strength of the overall stagnation point flow (of which k is a measure). The change in the stagnation ring position with pressure [Fig. 8(a)] arises from the increased volumetric flow rate into the orifice with increasing pressure. If the discharge coefficient (C_D) were constant, then the volumetric flow rate into the orifice would be constant (mass flow rate proportional to pressure), and the location of the stagnation ring would be independent of pressure. However, the discharge coefficient increases with increasing pressure (roughly as the square root of pressure, since the Reynolds number is proportional to pressure) and therefore the radius of the stagnation streamline increases with increasing pressure as well. This is a kinematic effect. The higher volumetric flow into the orifice at higher pressures leads to a larger region of streamlines entering the orifice. Likewise, the stagnation ring radius increases with increasing orifice diameter [Fig. 8(b)] because the volumetric flow rate into the orifice increases with the orifice diameter while the strength of the stagnation flow is unchanged. The volumetric flow rate increases roughly as $d^{2.5}$, since the Reynolds number is proportional to d (giving $C_D \propto d^{0.5}$), and the flow rate for an ideal choked flow is proportional to d^2. The discharge coefficient is nearly independent of the inlet velocity (u_0) so both the mass flow rate and volumetric flow rate into the orifice are unaffected by changes in the inlet velocity. The decrease in the stagnation ring radius with increasing inlet velocity [Fig. 8(c)] reflects the fact that for an increasing inlet flow rate (increasing strength of the stagnation point flow), the constant flow rate through the orifice is a decreasing fraction of the total flow. Changing the substrate temperature at fixed inlet temperature affects the flow into the orifice but does not affect the stagnation point flow. The flow rate into the orifice decreases roughly as $T_s^{-1/2}$, so the stagnation ring radius decreases as something like $T_s^{-1/8}$, consistent with the weak dependence observed in Fig. 8(d). Increasing the inlet temperature decreases the mass flow rate of the stagnation point flow, due to the decrease in the inlet density (with fixed inlet velocity). It has little effect on the flow into the orifice, since the density near the orifice is set by the substrate temperature. As the inlet temperature is increased, the flow into the orifice is an increasing fraction of the total flow, and the radius of the stagnation ring increases [Fig. 8(e)], roughly as $T_0^{1/4}$.

The axial extent of the sampling disturbance does not correlate directly with the radial extent. A good measure of the axial extent is the shift of the isotherm corresponding to the temperature at the center of the orifice. The isotherm shift (δ_T) is defined as the distance from the surface, at points radially far from the orifice, where the temperature is equal to the temperature at the center of the orifice entrance. If the energy balance equation (see Table I) is made dimensionless, and the terms corresponding to compressibility, reaction, and species diffusion are dropped, the Peclet number remains as the only dimensionless parameter in the equation. Therefore, when convection and conduction dominate the effects of compressibility and reaction, the solution will depend only on the Peclet number. In analogy to Eq. (1) and the work of Yi and Knuth,[22] we expect that the isotherm shift (δ_T) will be proportional to the square root of the Peclet number,

$$\frac{\delta_T}{d} = \alpha \, \mathrm{Pe}_h^{0.5}, \tag{9}$$

where Pe_h=Peclet number for heat transfer=Re Pr $=(\dot{m}C_p)/(\pi d\lambda)$, C_p= specific heat, λ=thermal conductivity, α=a constant of proportionality, taken to be 0.22 in this work.

Figure 9 compares the predictions of Eq. (9) to the values of δ_T obtained from examination of the detailed calculations. The scaling predicted by Eq. (9) is followed closely, except when the freestream temperature and the substrate temperature are close to each other, so that the system is nearly isothermal [see Fig. 9(e)]. If the temperature profile was determined solely by convection and conduction, then we would expect δ_T to depend only on the Peclet number. However, for nearly isothermal conditions, this is not the case. When the system is nearly isothermal, then the temperature gradients in the system are small, and therefore the conductive and diffusive terms in the energy equation are small. The terms in the energy equation corresponding to gas expansion do not depend on the temperature gradient, so they become relatively important under these conditions. Gas

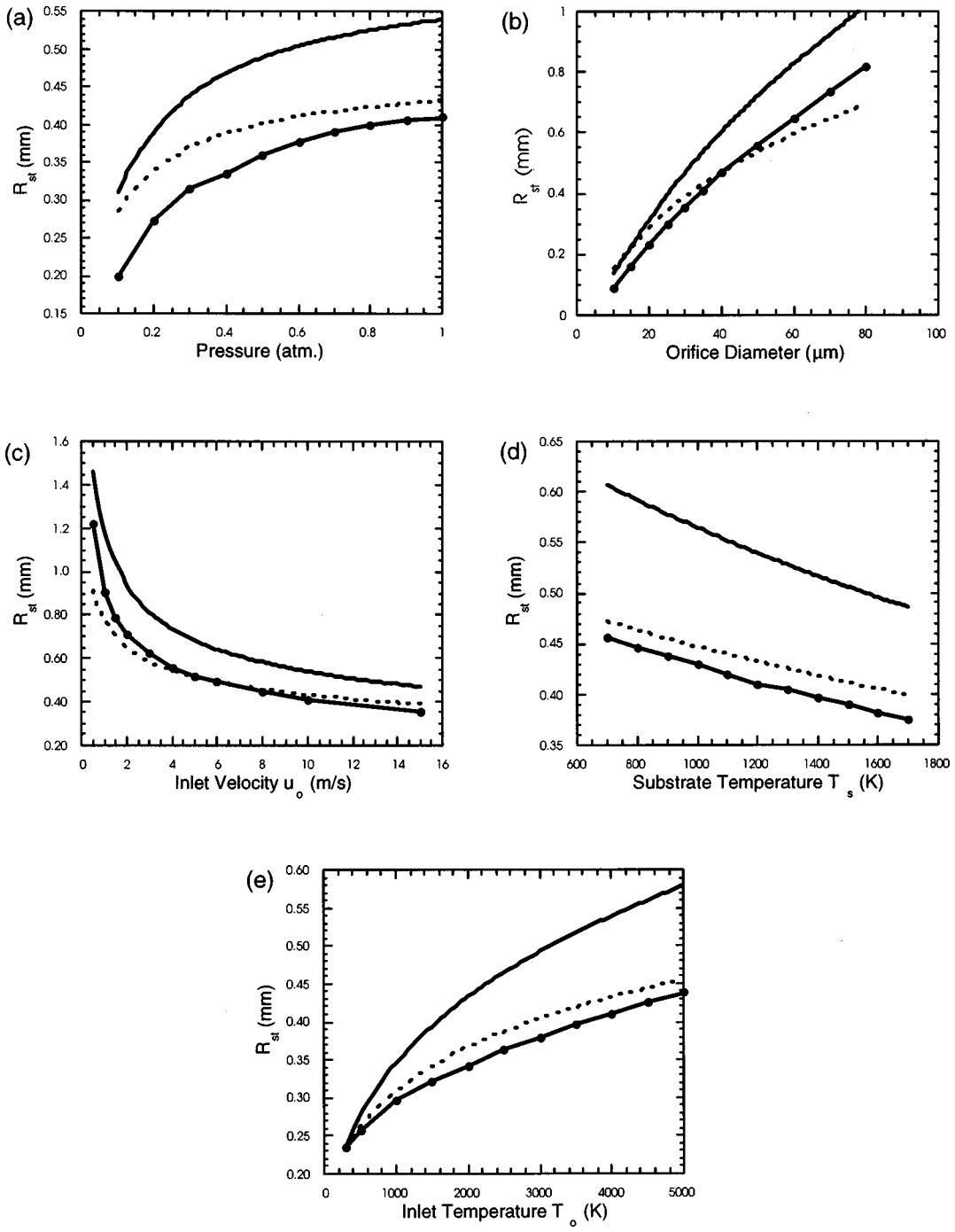

FIG. 8. Comparisons of the predicted location of the stagnation ring (R_{st}) predicted by scaling rules based on simplified streamfunctions to results of the detailed calculations. The solid line is from Eq. (5) and the dashed line is from Eq. (7) in the text. The filled circles connected by a solid line are the results of individual runs of the detailed simulations.

expansion cools the gas near the orifice, shifting the isotherms away from the orifice (less net shift toward the orifice) when the substrate temperature is lower than the inlet temperature and shifting the isotherms toward the orifice (more net shift) when the substrate temperature is higher than the inlet temperature. This is what is observed in Fig. 9(e).

Taken together, Eqs. (7) and (9) allow us to obtain semiquantitative estimates of the size of the disturbance due to the flow field. These may be compared to the thickness of the concentration and temperature boundary layers and the overall dimensions of the flow system to qualitatively evaluate the effect of sampling disturbance on measured species concentrations.

IV. SUMMARY AND CONCLUSIONS

Results of detailed two-dimensional reacting compressible flow calculations of gas sampling through an orifice during chemical vapor deposition were presented. Quantitative

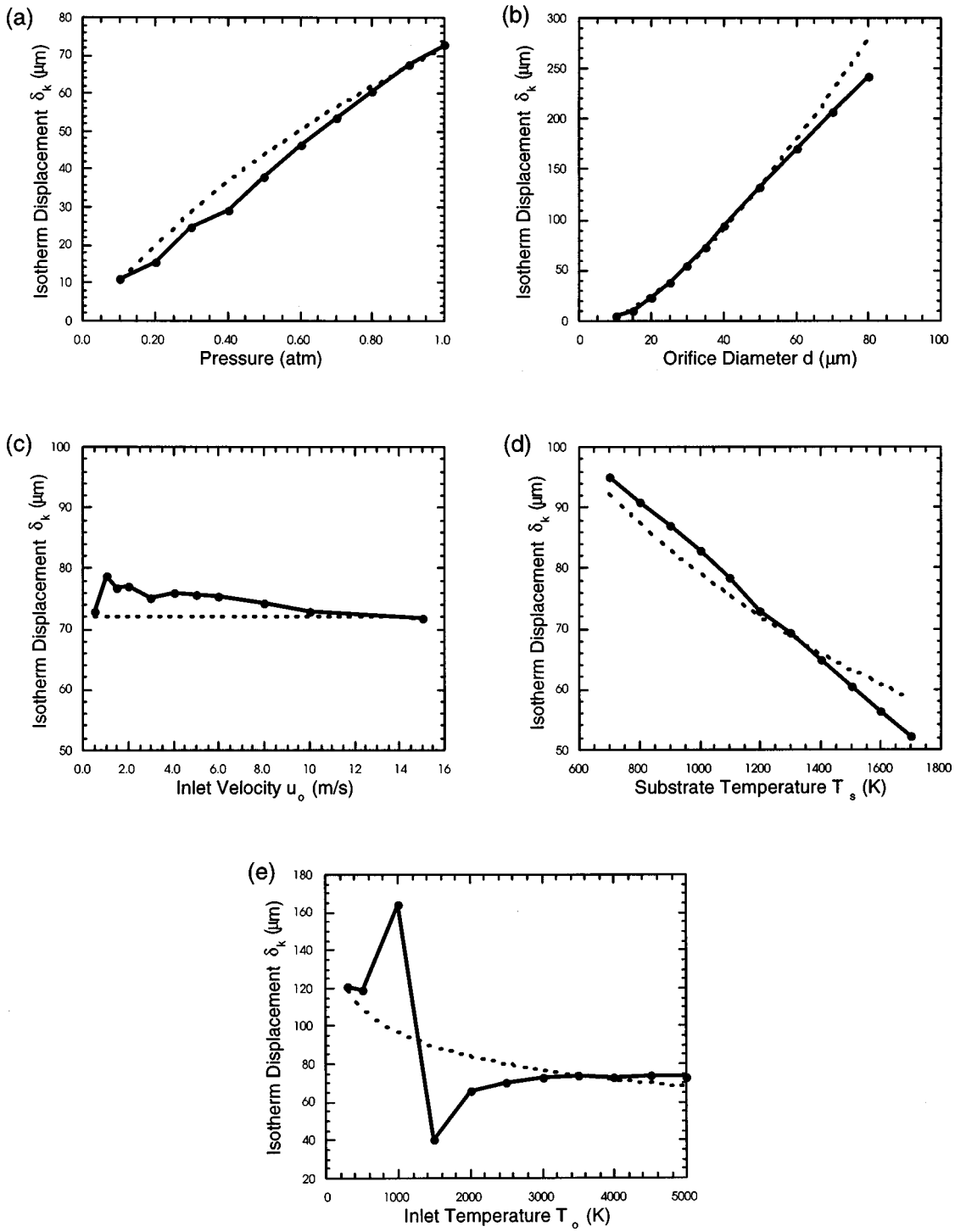

FIG. 9. Comparisons of the predicted shift in the isotherms from Eq. (9) in the text to results of the detailed calculations. The dashed line is from Eq. (9). The filled circles connected by a solid line are the results of individual runs of the detailed simulations.

results corresponding to atmospheric radiofrequency plasma CVD of diamond showed that these disturbances can be significant and can partially account for discrepancies between experimental concentration measurements and modeling results. Simplified streamfunctions were presented that closely approximate the flow field from the detailed calculations. Finally, scaling rules for the radial and axial extent of the sampling disturbance were presented and evaluated by comparison to the results of the detailed simulations over a range of operating conditions.

ACKNOWLEDGMENTS

This work was partially supported by National Science Foundation Grant No. CTS-9424271, by the Engineering Research Center on Plasma-Aided Manufacturing, and by the Minnesota Supercomputer Institute. The authors gratefully acknowledge contributions to this work by John Lindsay and John Larson in the form of helpful discussions, access to details of previous work, and assistance with the quasi-one-dimensional modeling.

[1]C. A. Wolden, R. F. Davis, Z. Sitar, and J. T. Prater, ''*In situ* mass spectrometry during diamond chemical vapor deposition using a low pressure flat flame,'' J. Mater. Res. **12**, 2733–2742 (1997).
[2]W. L. Hsu, M. C. McMaster, M. E. Coltrin, and D. S. Dandy, ''Molecular beam mass spectrometry studies of chemical vapor deposition of diamond,'' Jpn. J. Appl. Phys., Part 1 **33**, 2231–2239 (1994).
[3]P. G. Gruel, H. J. Yoon, D. W. Ernie, and J. T. Roberts, ''Mass spectrometric analysis of a high pressure, inductively coupled plasma during diamond film growth,'' Mater. Res. Soc. Symp. Proc. **334**, 141–146 (1994).
[4]S. L. Girshick and J. M. Larson, ''Thermal plasma synthesis of diamond,'' Pure Appl. Chem. **70**, 485–492 (1998).
[5]J. W. Lindsay, J. M. Larson, and S. L. Girshick, ''Effect of surface species concentrations and temperature on diamond film morphology in inductively coupled rf plasma CVD,'' Diamond Relat. Mater. **6**, 481–485 (1997).
[6]C. A. Wolden, G. Zau, W. T. Conner, H. H. Sawin, and K. K. Gleason, ''A novel molecular beam reactor for the study of diamond surface chemistry,'' Mater. Res. Soc. Symp. Proc. **334**, 123–128 (1994).
[7]I. B. Graff, Jr., R. A. Pugliese, and P. R. Westmoreland, ''Using molecular-beam mass spectrometry to study the PECVD of diamondlike carbon films,'' Mater. Res. Soc. Symp. Proc. **334**, 129–134 (1994).
[8]T. R. Gow, D. G. Coronell, and R. I. Masel, ''The mechanism of laser-assisted CVD of germanium,'' J. Mater. Res. **4**, 634–640 (1989).
[9]C. C. Amato, J. B. Hudson, and L. V. Interrante, ''Identification of the gas-phase products which occur during the deposition of AlN using the organometallic precursor $[CH_3)_2AlNH_2]$,'' Appl. Surf. Sci. **54**, 18–24 (1992).
[10]P. W. Lee, T. R. Omstead, D. R. McKenna, and K. F. Jensen, ''*In situ* mass spectrometry and thermogravimetric studies of GaAs MOCVD gas phase and surface reactions,'' J. Cryst. Growth **85**, 165–74 (1987).
[11]P. W. Lee, T. R. Omstead, D. R. McKenna, and K. F. Jensen, ''*In situ* mass spectroscopy studies of the decomposition of organometallic arsenic compounds in the presence of $Ga(CH_3)_3$ and $Ga(C_2H_5)_3$,'' J. Cryst. Growth **93**, 134–42 (1988).
[12]M. Yoshimoto, K. Takubo, T. Ohtsuki, M. Komoda, and H. Matsunami, ''Deposition mechanism of silicon nitride in direct photoassisted chemical vapor deposition using a low-pressure Hg lamp,'' J. Electrochem. Soc. **142**, 1976–82 (1995).
[13]P. A. C. Groenen, J. G. A. Hölscher, and H. H. Brongersma, ''Mechanism of the reaction of WF_6 and Si,'' Appl. Surf. Sci. **78**, 123–32 (1994).
[14]E. Golusda, R. Lange, K.-D. Lühmann, G. Mollekopf, M. Wacker, and H. Stafast, ''CW CO_2 laser CVD of amorphous hydrogenated silicon (*a*-Si:H): Influence of the deposition geometry,'' Appl. Surf. Sci. **54**, 30–34 (1992).
[15]M. E. Coltrin, R. J. Kee, G. H. Evans, E. Meeks, F. M. Rupley, and J. F. Grcar, ''Spin: A FORTRAN program for modeling one-dimensional rotating-disk/stagnation-flow chemical vapor deposition reactors,'' Sandia National Laboratories, Report No. SAND91-8003, 1991.
[16]B. W. Yu and S. L. Girshick, ''Atomic carbon vapor as a diamond growth precursor in thermal plasmas,'' J. Appl. Phys. **75**, 3914–3923 (1994).
[17]S. L. Girshick, C. Li, B. W. Yu, and H. Han, ''Fluid boundary layer effects in atmospheric-pressure plasma diamond film deposition,'' Plasma Chem. Plasma Process. **13**, 169–187 (1993).
[18]J. W. Lindsay, ''A study of gas phase chemistry during RF thermal plasma diamond deposition,'' Ph.D. dissertation, University of Minnesota, 1998.
[19]A. N. Hayhurst, D. B. Kittelson, and N. R. Telford, ''Mass spectrometric sampling of ions from atmospheric pressure flames II: Aerodynamic disturbance of a flame by the sampling system,'' Combust. Flame **28**, 123–135 (1977).
[20]A. N. Hayhurst and D. B. Kittelson, ''Mass spectrometric sampling of ions from atmospheric pressure flames-III: Boundary layer and other cooling of the sample,'' Combust. Flame **28**, 137–143 (1977).
[21]A. N. Hayhurst and N. R. Telford, ''Mass spectrometric sampling of ions from atmospheric pressure flames-I: Characteristics and calibration of the sampling system,'' Combust. Flame **28**, 67–80 (1977).
[22]A. C. Yi and E. L. Knuth, ''Probe-induced concentration distortions in molecular-beam mass-spectrometer sampling,'' Combust. Flame **63**, 369–379 (1986).
[23]E. L. Knuth, ''Composition distortion in MBMS sampling,'' Combust. Flame **103**, 171–180 (1995).
[24]O. I. Smith, ''Probe sampling from combustion systems,'' in *Flame Structures and Processes*, edited by R. M. Fristrom (Oxford University Press, Oxford, 1995), pp. 168–195.
[25]CFD-ACE Command Language Reference Manual, version 2.1, CFDRC Report No. GR-97-30, CFD Research Corporation, Huntsville, AL, 1997.
[26]S. V. Patankar, *Numerical Heat Transfer and Fluid Flow* (Hemisphere, Washington, 1980).
[27]J. O. Hirschfelder, C. F. Curtiss, and R. B. Bird, *Molecular Theory of Gases and Liquids* (Wiley, New York, 1954).
[28]R. J. Kee, G. Dixon-Lewis, J. Warnatz, M. E. Coltrin, and J. A. Miller, ''A FORTRAN computer code package for the evaluation of gas-phase, multicomponent transport properties,'' Sandia National Laboratories Report No. SAND86-8246, 1986.
[29]R. J. Kee, F. M. Rupley, and J. A. Miller, ''The CHEMKIN thermodynamic database,'' Sandia National Laboratories Report No. SAND-87-8215B, 1990.
[30]M. E. Coltrin, R. J. Kee, and F. M. Rupley, ''Surface CHEMKIN: A general formalism and software for analyzing heterogeneous chemical kinetics at a gas-surface interface,'' Int. J. Chem. Kinet. **23**, 1111–1128 (1991).
[31]J. M. Larson, M. T. Swihart, and S. L. Girshick, submitted to Diamond Relat. Mater.
[32]N. J. Brown, G. Li, and M. L. Koszykowski, ''Mechanism reduction via principal component analysis,'' Int. J. Chem. Kinet. **29**, 393–414 (1997).
[33]C. T. Bowman, R. K. Hanson, D. F. Davidson, W. C. Gardiner, Jr., V. Lissianski, G. P. Smith, D. M. Golden, M. Frenklach, and M. Goldenberg, ''GRI-Mech 2.11,'' http://www.me.berkeley.edu/grimech/,'' Gas Research Institute, 1998.
[34]S. J. Harris, ''Mechanism for diamond growth from methyl radicals,'' Appl. Phys. Lett. **56**, 2298–2300 (1990).
[35]B. K. Hodge and Keith Koenig, *Compressible Fluid Dynamics* (Prentice–Hall, Englewood Cliffs, 1995).
[36]W. B. Brower, E. Eisler, E. J. Filkorn, J. Gonenc, P. Plati, and J. Stagnitti, ''On the compressible flow through an orifice,'' J. Fluids Eng. **115**, 660–664 (1993).
[37]H. P. Liepmann, ''Gas kinetics and gas dynamics of orifice flow,'' J. Fluid Mech. **10**, 65–79 (1961).